

PCCP

Accepted Manuscript



This is an *Accepted Manuscript*, which has been through the Royal Society of Chemistry peer review process and has been accepted for publication.

Accepted Manuscripts are published online shortly after acceptance, before technical editing, formatting and proof reading. Using this free service, authors can make their results available to the community, in citable form, before we publish the edited article. We will replace this *Accepted Manuscript* with the edited and formatted *Advance Article* as soon as it is available.

You can find more information about *Accepted Manuscripts* in the [Information for Authors](#).

Please note that technical editing may introduce minor changes to the text and/or graphics, which may alter content. The journal's standard [Terms & Conditions](#) and the [Ethical guidelines](#) still apply. In no event shall the Royal Society of Chemistry be held responsible for any errors or omissions in this *Accepted Manuscript* or any consequences arising from the use of any information it contains.

Spectral lineshapes in nonlinear electronic spectroscopy[†]

Artur Nenov,^{*a} Angelo Giussani,^a Benjamin P. Fingerhut,^b Ivan Rivalta,^c
Elise Dumont,^c Shaul Mukamel,^d and Marco Garavelli^{*a,c}

Received Xth XXXXXXXXXXXX 20XX, Accepted Xth XXXXXXXXXXXX 20XX

First published on the web Xth XXXXXXXXXXXX 200X

DOI: 10.1039/b000000x

We outline a computational approach for nonlinear electronic spectra, which accounts for the electronic energy fluctuations due to nuclear degrees of freedom and explicitly incorporates the fluctuations of higher excited states, induced by the dynamics in the photoactive state(s). The approach is based on mixed quantum-classical dynamics simulations. Tedious averaging over multiple trajectories is avoided by employing the linearly displaced Brownian harmonic oscillator to model the correlation functions. The present strategy couples accurate computations of the high-lying excited state manifold with dynamics simulations. Application is made to the two-dimensional electronic spectra of pyrene, a polycyclic aromatic hydrocarbon characterized by an ultrafast (few tens of femtosecond) decay from the bright S₂ state to a dark S₁ state. The spectra for waiting times $t_2 = 0$ and $t_2 = 1$ ps demonstrate the ability of this approach to model electronic state fluctuations and realistic lineshapes. Comparison with experimental spectra [Krebs *et al.*, *New Journal of Physics*, 2013, **15**, 085016)] shows excellent agreement and allows to unambiguously assign the excited state absorption features.

1 Introduction

When studying ultrafast excited state (ES) dynamics with transient spectroscopy techniques one must consider dephasing processes which occur on a time scale comparable to the delay time between the pulses. The recorded spectra provide an averaged picture of the dynamics during the measurement (which can last several hundreds of femtoseconds). Nevertheless, the high temporal resolution (down to 5-10 femtoseconds) stems from the fact that different segments of the dynamics

[†] Electronic Supplementary Information (ESI) available: Molecular orbitals of pyrene, electronic structure of the Franck-Condon point, geometrical parameters and Cartesian coordinates of relevant structures. See DOI: 10.1039/b000000x/

^a Dipartimento di Chimica G. Ciamician, Università di Bologna, V. F. Selmi 2, 40126 Bologna, Italy. Tel: +390512099495; E-mail: artur.nenov@unibo.it; marco.garavelli@unibo.it

^b Max Born Institute for Nonlinear Optics and Short Pulse Spectroscopy, Max-Born-Strasse 2A, 12489, Berlin, Germany.

^c Laboratoire de Chimie, Ecole Normale Supérieure de Lyon, 46, allée d'Italie 69364 Lyon, France.

^d Department of Chemistry, University of California, Irvine, California 92697-2025, United States.

are averaged over depending on the delay times between the laser pulses which interact with the sample. To account for this time averaging in theoretical spectroscopy it is crucial to model electronic fluctuations due to nuclear degrees of freedom, either intra- or intermolecular (i.e. the spectral diffusion), and the fluctuations of the respective oscillator strengths during the underlying ultrafast dynamics¹⁻⁴.

Another essential requirement for modeling nonlinear spectra of photoexcited molecules is the incorporation of higher lying ES. This is desirable for two reasons: first, absorptions to these states (excited state absorptions, ESA) dominate the spectra due to the high spectral density in the visible (Vis) and ultraviolet (UV)⁵⁻⁷; second, ESA, together with the stimulated emission (SE) represent characteristic signatures of each photophysical or photochemical decay channel, hence, their proper description will allow to recognize electronic structure changes during the dynamics, as well as to disentangle dynamics occurring via competing channels⁸. However, the higher ES also exhibit fluctuations coupled to the dynamics on the states on which the relevant photophysics and photochemistry occur (i.e. the photoactive states). An approach is desired which accounts for these fluctuations in the simulation of the nonlinear spectra. The accurate and complete computation of the higher ES manifold is challenging by itself and we demonstrated recently that a significant amount of preliminary work (related to calibrating the computational methods), as well as time and resource consuming computations is required to obtain useful results^{5,9,10}. The high cost of performing excited state computations drew our attention towards exploring approximate methods for describing photoinduced events.

In this report we present an efficient way of incorporating nuclear dynamics in nonlinear electronic

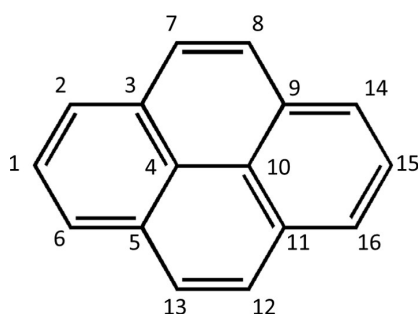


Fig. 1 Pyrene structure with atom labels.

spectroscopy within the framework of mixed quantum-classical dynamics. We use a mathematical model that relies on the cumulant expansion, describing the system's nonlinear response to the electric field, and utilizes a single trajectory as input in combination with state-of-the-art electronic structure computations to describe contributions due to coherent nuclear motion. We discuss different approximation levels with their limitations. We resort to pump-probe and two-dimensional (2D) electronic spectroscopy (third-order nonlinear techniques) with broadband probing in the Vis-to-UV in order to assess the accuracy of the presented approach. Notably, 2D optical spectroscopy, which is now state of the art in the infrared regime, is becoming accessible in the Vis and UV¹¹⁻¹⁸ and has recently been coupled to supercontinuum probing¹⁹. The beauty of supercontinuum probing resides in its ability to resolve multiple ESA transitions and track their evolution over time. This is a crucial requirement for electronic spectroscopy, as we have shown in previous works that the

most characteristic ESA and SE signals can exhibit shifts of several thousands of cm^{-1} during the dynamics^{7,8}.

Recently, Riedle and co-workers reported the 2D spectrum of pyrene, a polycyclic aromatic hydrocarbon, obtained by pumping at the frequency of the bright electronic transition to the second excited state S_2 around 32000 cm^{-1} and utilizing a supercontinuum probe in the region $16000\text{-}38000 \text{ cm}^{-1}$ after a waiting time of 1 ps ¹⁹. The spectrum is characterized by a vibronic progression of ground state bleach (GSB) peaks and several well-resolved ESA bands. Using the introduced approach we simulate 2D spectra of pyrene for waiting times $t_2 = 0$ and $t_2 = 1 \text{ ps}$.

2 Single-trajectory based approach for 2D electronic spectroscopy

Multiple field-matter interactions create higher order (nonlinear) responses. The experimental set-up for 2D electronic spectroscopy uses three pulses with wavevectors k_1 , k_2 and k_3 which interact with the system. The third order nonlinear polarization emits a signal along a given phase-matched direction which is superimposed with a fourth pulse known as the local oscillator (LO). The third-order heterodyne signal^{20,21}

$$S^{(3)}(t_1, t_2, t_3) = \int_{-\infty}^{\infty} dt \int_0^{\infty} dt_1 \int_0^{\infty} dt_2 \int_0^{\infty} dt_3 R^{(3)}(t_1, t_2, t_3) \times \mathbf{E}(r, t) \mathbf{E}(r, t - t_1) \mathbf{E}(r, t - t_1 - t_2) \mathbf{E}(r, t - t_1 - t_2 - t_3) \quad (1)$$

involves three temporally separated interactions with the electric field $\mathbf{E}(r, t) = E(t)e^{i\mathbf{k}r - i\omega t}$ with central frequency ω and a complex envelope $E(t)$. $S^{(3)}(t_1, t_2, t_3)$ depends parametrically on the delay times t_1 , t_2 and t_3 between the field-matter interactions. The time-dependent signal is Fourier-transformed along t_1 and t_3 (i.e. delay times) to obtain the 2D spectrum for each waiting time t_2 . In the following we work in the semi-impulsive limit, in which the envelopes of the pulses are approximated by a δ -function. In this limit the emitted signal becomes proportional to the nonlinear response²²

$$R^{(3)}(t_1, t_2, t_3) = i^3 \text{Tr}[\hat{\mu} \mathbb{G}(t_3) [\hat{\mu}, \mathbb{G}(t_2) [\hat{\mu}, \mathbb{G}(t_1) [\hat{\mu}, \rho(0)]]]] \quad (2)$$

where $\rho(0)$ is the equilibrium density matrix of the system in the basis of the nuclear amplitudes $\chi_i(t, Q)$, i.e. the expansion coefficients of the wavefunction $\Psi(t, Q, r)$ of the quantum-mechanical system

$$\Psi(t, Q, r) = \sum_i \chi_i(t, Q) \Phi_i(r; Q), \quad (3)$$

formulated in the basis of the electronic wavefunctions $\Phi_i(r; Q)$. The latter are parametrically dependent on the nuclear coordinates Q and can be formulated either in the adiabatic or in the diabatic basis. For the electronic states $\Phi_i(r; Q)$ we consider the GS g , the manifold of singly ESs e , accessible through the pump pulse (pair), and the manifold of higher lying states f . The field-free propagation of the density matrix $\rho(t)$ is governed by the retarded Green's function

$$\mathbb{G}(t)\rho(0) = \Theta(t)e^{-i\hat{H}t}\rho(0)e^{i\hat{H}t} = \rho(t) \quad (4)$$

with the vibronic Hamiltonian $\hat{H} = \sum_{ij} |\chi_i\rangle \left(\hat{T}^{nuc} \delta_{ij} + V_{ij} + \hat{T}_{ij} \right) \langle \chi_j|$. \hat{T}^{nuc} is the nuclear kinetic energy operator. $V_{ij} = \langle \Phi_i(r; Q) | \hat{H}^{el} | \Phi_j(r; Q) \rangle$ is an element of the electronic Hamiltonian matrix which becomes diagonal in the adiabatic electronic wavefunction basis, i.e. $V_{ij} = V_i \delta_{ij}$, with the adiabatic electronic potential V_i being the i -th eigenvalue of the electronic Hamilton operator \hat{H}^{el} at the nuclear position Q . $\hat{T}_{ij} = (2m)^{-1} d_{ij} \nabla_Q$ is the non-adiabatic coupling term with elements d_{ij} the non-adiabatic coupling vectors²³, which are absent in the diabatic representation. $\Theta(t)$ denotes the Heaviside step-function ensuring causality.

Before the interaction with the first pulse in eq. 2 $\rho(t)$ is in the GS equilibrium (i.e. $\rho(0) = |\chi_g\rangle \langle \chi_g|$). The interaction with the laser pulses enters eq. 2 through the coordinate dependent transition dipole moment $\hat{\mu} = \sum_{ij} |\chi_i\rangle \mu_{ij}(\tau) \langle \chi_j|$ which couples states i and j . The time argument τ serves merely to indicate the time of interaction with the laser pulse. Following relations hold: $\tau_1 = 0$, $\tau_2 = \tau_1 + t_1$, $\tau_3 = \tau_2 + t_2$, $\tau = \tau_3 + t_3$. The expression in eq. 2 gives rise to eight different interaction sequences of the incident electric fields with the system, known as Feynman pathways. A suitably positioned detector can be used to select pathways subject to a phase-matching condition. Exemplarily, in the rephasing k_I ($k_{LO} = -k_1 + k_2 + k_3$) phase-matching condition pathways corresponding to GS bleach (GSB), ES absorption (ESA) and stimulated emission (SE) are simultaneously recorded.

$$R_{\mathbf{k}_I}^{(3)}(t_1, t_2, t_3) = \sum_{i=GSB,SE,ESA} R_{\mathbf{k}_I,i}^{(3)}(t_1, t_2, t_3). \quad (5)$$

Before we proceed with re-writing eq. 2 within the framework of mixed quantum-classical dynamics, we briefly describe how nuclear and electronic dynamics are treated therein. The quantum system is expressed as a linear combination of adiabatic wavefunctions $\Phi_i(r; Q)$

$$\Psi(t, Q, r) = \sum_i c_i(t) \Phi_i(r; Q). \quad (6)$$

Note, that the time-dependent expansion coefficients $c_i(t)$ in eq. 6, unlike the nuclear amplitudes $\chi_i(t, Q)$ (eq. 3), have no explicit dependence on the nuclear coordinates Q . In the basis of the coefficients $c_i(t)$ an element of the density matrix becomes $\rho_{ij}(t) = c_i(t) c_j^*(t)$ ²⁴⁻²⁶. After inserting the wavefunction (eq. 6) in the time-dependent Schrödinger equation one obtains the equations of motion for the electronic degrees of freedom^{27,28}

$$i\dot{c}_i(t) = \sum_j \left(V_{ij} - i d_{ij} \dot{Q} \right) c_j(t) \quad (7)$$

while the nuclear degrees of freedom are described using the classical Newtonian law of motion

$$m\ddot{Q} = \mathfrak{F} = -\langle \Psi(t, Q, r) | \nabla_Q \hat{H}^{el} | \Psi(t, Q, r) \rangle \quad (8)$$

with \mathfrak{F} the force of the quantum-mechanical system on the classical bath. \dot{Q} in eq. 7 and \ddot{Q} in eq. 8 denote the nuclear velocity and acceleration vectors. In a semi-classical, trajectory based Ansatz, the coupled eqs. 7 and 8 are commonly solved applying the independent trajectory approximation, where each trajectory is driven by a single electronic potential (the force \mathfrak{F} in eq. 8 is then simply given by the gradient on a single electronic potential $\Phi_i(r; Q)$). The probability distribution is recovered in a

stochastic manner by allowing the trajectories to change the surface on which they are evolving (i.e. a surface hopping event²⁹). Thereby, the decision of working either in the adiabatic or in the diabatic representation is taken based on the availability of non-adiabatic elements (necessary for adiabatic dynamics) or adiabatic-to-diabatic transformation matrix (necessary for diabatic dynamics).

The stochastic nature of surface hopping makes it meaningless within the single trajectory framework. Therefore, we are forced to restrict the dynamics on a single electronic state and to neglect inter-state couplings when relying on a single trajectory. This simplifies the electronic equations of motion 7 to a set of independent equations

$$i\dot{c}_i(t) = E_i c_i(t). \quad (9)$$

Eq. 9 is written in a general basis, where E_i can correspond either to an eigenvalue of the electronic Hamilton operator \hat{H}_{el} (adiabatic representation) or to a diagonal element of the electronic Hamiltonian matrix V (diabatic representation). At that point we note that, while the outcome of the mixed quantum-classical dynamics simulations following eq. 7 does not depend on the choice of basis, this is no longer the case in the single trajectory framework utilizing eq. 9. Performing adiabatic dynamics, while neglecting the non-adiabatic coupling vectors d_{ij} , allows for ultrafast changes of the ES wavefunction. On the other hand, diabatic dynamics in the absence of diabatic couplings V_{ij} implies to follow the nature of the ES. In the following we will formulate the equations for the nonlinear response in the general basis. For practical applications one has to estimate which representation poses a smaller approximation in the description of the ultrafast dynamics in the system of interest. This aspect is further discussed in the Computational Methods, relating it to pyrene.

Having worked out the basics of mixed-quantum classical dynamics in the single trajectory framework we now proceed to re-formulate eq. 2. We consider a system consisting of a single bright state e which is vibronically coupled to one or more dark states e' , as is the situation in pyrene (see Results). The density matrix $\rho(t)$ is propagated according to the coupled equations of motion for the electrons and nuclei. With eq. 9 the propagation of the density matrix when the system is in a coherence state, i.e. $\rho(t) = c_i(t)c_j^*(t)$, simplifies to a function of the fluctuating electronic gap between the states i and j

$$\rho(t) = \mathbb{G}(t)\rho(0) = \Theta(t)\rho(0)e^{-i\int^t(E_i(\tau')-E_j(\tau'))d\tau'}. \quad (10)$$

The choice of a reference Hamiltonian acting on the classical bath (eq. 8) during a coherence propagation, as it is the case during the delay times t_1 and t_3 (Fig. 2), is not unique^{2,20} as the bra and the ket side of the density matrix are subject to different electronic potentials. During coherence between the GS g and the singly excited manifold e , as well as between the singly ES manifold e and the higher ES manifold f we choose to propagate the nuclear degrees of freedom as if interacting with the singly excited electronic state e . Subotnik and co-workers proposed recently to use a swarm of trajectories propagated independently in the GS and in the ES³, thereby introducing two different reference Hamiltonians for either the bra or ket side and evaluating the coherence as the geometric average.

The above approximation allows to derive a simplified expression for each Feynman pathway (eq. 5). Exemplarily, the response function $R_{\mathbf{k}_1,ESA}^{(3)}(t_1, t_2, t_3)$ for the ESA for the rephasing phase-matching

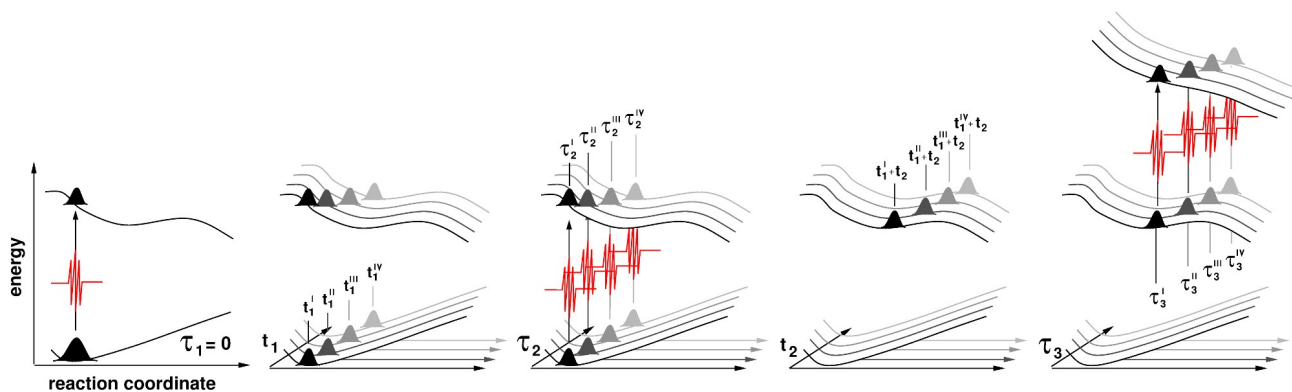


Fig. 2 Schematic representation of the ES absorption signal in 2D electronic spectroscopy. The approximation of coherent superposition dynamics during the delay times t_1 and t_3 assumes that the wavepacket superpositions, created by the first pump pulse at time τ_1 and the probe pulse at time τ_3 , evolve coherently on two electronic potentials and nuclear decoherence effects are neglected. For each combination of delay time t_1 and waiting time t_2 the population (color coded and labeled), generated upon interaction with the second pump pulse at time τ_2 , has propagated coherently on the electronic potentials, so that the third pulse probes a different segment of the higher ES manifold. The time-dependent fluctuation of the electronic gap is a function of (and hence contains information about) the active vibrational modes. In the semi-impulsive limit the signal intensity depends on the magnitude of the transition dipole moment at times τ_1 , τ_2 and τ_3 .

condition reads

$$R_{\mathbf{k}_1, ESA}^{(3)}(t_1, t_2, t_3) = \text{Tr}[\hat{\mu}\mathbb{G}(t_3)(\hat{\mu}\mathbb{G}(t_2)(\hat{\mu}\mathbb{G}(t_1)(\rho(0)\hat{\mu})))] = i\Theta(t_1)\Theta(t_2)\Theta(t_3) \sum_f \mu_{ef}(\tau) \mu_{fe}(\tau_3) \mu_{eg}(\tau_2) \mu_{ge}(\tau_1) e^{-i \int^{\tau_1} (E_e(\tau') - E_g(\tau')) d\tau' - t_1/T_e} e^{-t_2/T_e} e^{-i \int^{t_3} (E_f(\tau') - E_e(\tau')) d\tau' - t_3/T_e} \quad (11)$$

where the infinite ES lifetime (a consequence of eq. 9) is corrected phenomenologically by introducing an effective ES lifetime T_e . During the waiting time t_2 the system is in a population state $\rho(t_2) = c_e(t_2)c_e^*(t_2)$, exhibiting coherent population dynamics modulated by T_e . Eq. 11 (and its GSB and SE counterparts, which we do not explicitly formulate here) take into account the electronic fluctuations due to nuclear motion in the ES (i.e. spectral diffusion) and can be directly employed for the simulation of 2D electronic signals by a 2D Fourier-transformation of the third order response function $R^{(3)}(t_1, t_2, t_3)$ subject to field envelopes with respect to time delays t_1 and t_3 (eq. 1), followed by averaging over an ensemble of trajectories. On the single trajectory level the Fourier-transformation can introduce dispersive contributions in the spectra if the electronic gap fluctuations induce a shift of the mean transition frequency within the dephasing timescale³⁰. The dispersive features are (in part) averaged out in the ensemble averaged signal. This effect is particularly severe for large energetic fluctuations and ultrashort time-scale dynamics.

The cumulant expansion provides an exact solution to models with Gaussian statistics, i.e. the electronic degrees of freedom coupled to a harmonic bath. The Ansatz avoids tedious averaging over trajectories by introducing a functional form for the correlation function. By introducing the

harmonic approximation, the linearly displaced Brownian harmonic oscillator model (BHO) thus represents an analytical solution of the coherence evolution for two (e.g. GS and ES) multidimensional harmonic oscillators^{3,20}. It provides an elegant alternative to extract relevant information for the spectral lineshape function $g(t)$ from a single trajectory. The use of the BHO model is generally justified as the FC active modes that control the immediate relaxation after excitation are associated with bond relaxation deformations, whose GS and ES can be described to a good approximation through displaced harmonic potentials (short time approximation). ES specific structural deformations, which introduce anharmonicities in the potentials are generally activated on a longer time scale. The coherence dynamics $\sigma_{ij}(t) = e^{-i \int^t (E_i(\tau') - E_j(\tau')) d\tau'}$ (eq. 10) can be expressed within the BHO model as

$$\sigma_{ij}(t) = e^{-i\omega_{ij}t + g(t)} \quad (12)$$

with

$$g(t) = -i \sum_k D_k \int_0^t e^{-i\omega_k \tau'} d\tau'. \quad (13)$$

ω_{ij} refers to the adiabatic transition between the GS and the ES (i.e. ω_{eg}), while ω_k and D_k describe the frequencies of the active vibrational modes and their amplitudes (i.e. the Franck-Condon coefficients). Upon integration eq. 13 yields for coherent nuclear motion (underdamped limit)

$$g(t) = \sum_k S_k [(coth(\beta\hbar\omega_k/2)) (1 - \cos(\omega_k t)) + i(\sin(\omega_k t) - \omega_k t)] \quad (14)$$

where we have omitted the temperature dependence in eq. 13 (high frequency limit: $\beta\hbar\omega_k/2 > 1$ with inverse temperature $\beta = 1/k_B T$). The coefficients D_k are related to the Huang-Rhys factors S_k by the mean square displacement d of oscillator k ($D_k = 0.5d_k^2\omega_k$; $S_k = 0.5d_k^2$). In practice, ω_k and D_k are extracted from the ES trajectory (see Computational Methods).

Using eq. 12 the expression for the response function $R_{\mathbf{k}_1, ESA}^{(3)}(t_1, t_2, t_3)$ (eq. 11) becomes

$$R_{\mathbf{k}_1, ESA}^{(3)}(t_1, t_2, t_3) = i\Theta(t_1)\Theta(t_2)\Theta(t_3) \sum_f |\mu_{fe}(\tau_3)|^2 |\mu_{eg}|^2 e^{-i\omega_{eg}t_1 + g(t_1) - \Gamma t_1} e^{-t_2/T_e} e^{-i \int^{t_3} (E_f(\tau') - E_e(\tau')) d\tau' - \Gamma t_3}. \quad (15)$$

The Condon approximation applies for μ_{ge} during the coherence time t_1 , while the coordinate dependence of μ_{ef} is considered explicitly through the dependence of the transition dipole moment on the dynamics during the delay time t_1 and the waiting time t_2 . Besides the coherent nuclear motion and the ES lifetime, solvent induced fluctuations provide additional mechanisms of line broadening. While appearing naturally in the multi-trajectory description, the coherence decay due to these fluctuations must be introduced phenomenologically in the single trajectory framework. When these fluctuations are small or very fast, the fast modulation limit applies, i.e. the lineshape function simplifies to a homogenous Lorentzian characterized by the pure dephasing rate γ . The total homogenous dephasing contribution to the response function is thus given by $\Gamma = \gamma + 1/T_e$ in eq. 15. Eq. 15 applies for generating spectra based on a single trajectory simulation. It is particularly beneficial for simulating transient spectroscopy in the case of ultrafast dynamics during the delay times t_1 and t_2 , as it captures the spectral fluctuations and intensity modulation of the accessible

(i.e. bright) states in the higher ES manifold f which depend on the dynamics on the photoactive ES e . However, it must be noted that signals arising from other electronic states populated during the coherent dynamics are not incorporated in eq. 15, therefore the transient signal characterizes with an overall intensity decrease for longer waiting times t_2 as a consequence of the finite ES lifetime. The nonlinear response functions for GSB and SE can be formulated in a straight-forward way. The GSB reads

$$R_{\mathbf{k}_I, GSB}^{(3)}(t_1, t_2, t_3) = -i\Theta(t_1)\Theta(t_2)\Theta(t_3)|\mu_{eg}|^4 e^{-i\omega_{eg}t_1+g(t_1)-\Gamma t_1} e^{-i\omega_{eg}t_3+g(t_3)-\Gamma t_3}. \quad (16)$$

We note that the present model does not include GSB recovery. The SE reads

$$R_{\mathbf{k}_I, SE}^{(3)}(t_1, t_2, t_3) = -i\Theta(t_1)\Theta(t_2)\Theta(t_3)|\mu_{eg}(\tau_3)|^2 |\mu_{eg}|^2 e^{-i\omega_{eg}t_1+g(t_1)-\Gamma t_1} e^{-t_2/T_e} e^{-i\int^{t_3} (E_e(\tau')-E_g(\tau'))d\tau'-\Gamma t_3}. \quad (17)$$

In the Results section eqs. 15-17, together with their counterparts for the non-rephasing phase matching condition k_{II} ($k_{LO} = +k_1 - k_2 + k_3$), are used to simulate the absorptive two-dimensional spectrum^{20,21} of pyrene, as well as its marginal, the pump-probe spectrum, for waiting time $t_2 = 0$, thereby resolving the spectral features of the bright second ES S_2 .

Going beyond the restrictions posed by the introduced approach, namely, to provide the spectral lineshapes of ESA and SE associated only with the initially excited state, one faces the challenge of correlating non-equilibrium dynamics on different ESs subject to the inter-state couplings between them. In the special case when the fast initial dynamics in the bright state e due to the departure from the FC region is followed by slow dynamics associated with trapping of the ES population in dark states e' the non-linear response for waiting times t_2 longer than the ES lifetime T_e of the bright state e will be dominated by the ESA features of the ES intermediates. This allows to couple short-time ES dynamics, serving to describe the $g - e$ coherence during t_1 , with a static description of the $e' - f$ coherences during t_3 . In the static (snapshot) formulation of the nonlinear response it is assumed that the coherence dynamics is slower than the duration of the experiment and, therefore, spectral diffusion can be neglected. Therefore, one can use the energies obtained at the equilibrium geometry of the dark state to probe its ESA. The spectral lineshape at longer times is described solely through the homogenous dephasing rate. In principle population transfer among states could be incorporated either phenomenologically by a rate equation system²² or by microscopic surface hopping dynamics².

The coupling of fast and slow dynamics is particularly suitable for disentangling ES deactivation pathways through constructing the fingerprint spectra of the ES intermediates, which could be populated during the decay of the initially excited states. In the Results section we demonstrate how the idea can be applied in practice by coupling the short-time dynamics in the bright second ES of pyrene to the ESA spectrum of the local minimum on the dark first ES. The latter is known to be populated on a ultra-short time scale ($T_2 \approx 80$ fs).

3 Computational methods

The present study integrates different types of computations: ground and excited state optimizations, single point calculations, mixed quantum-classical dynamic simulations and the construction

of linear and nonlinear electronic spectra.

The calculations aimed at the characterization of the electronic structure of pyrene have been performed in the framework of the complete active space self-consistent field (CASSCF) approach^{31,32} augmented by second order perturbation theory (CASPT2)^{33,34}. We also made use of the restricted active space (RAS) variation of the scheme (i.e. RASSCF/RASPT2)³⁵ which constructs the list of configuration state functions through a limited number of simultaneously excited electrons out of the occupied orbital set RAS1 and a limited number of simultaneous excitations into the virtual orbital set RAS3, while still allowing for all possible permutations of electrons among the orbitals in the RAS2 set. In the particular application the RAS2 was left empty. We introduce the active space notation $\text{RAS}(n, m|0, 0|n, m)$, where n is the maximal number of simultaneously allowed holes(electrons) among the occupied(virtual) orbitals m in RAS1(RAS3). The optimization of the ground state was performed at CAS(4,4) level of theory, including the highest occupied molecular orbital (HOMO, H), the lowest unoccupied molecular orbital (LUMO, L), H-1 and L+1 and the corresponding electrons. The two lowest excited states of the system (the so-called L_a and L_b states in Platt's notation³⁶) were optimized within D_{2h} symmetry, with the π -orbitals and electrons of pyrene (see Supplementary Information †, Figure S1) distributed among the RAS1 and RAS3 subspaces and allowing up to quadruple excitations, i.e. $\text{RASSCF}(4, 8|0, 0|4, 8)$. The minimum on the dark state L_b was subsequently characterized by means of single point calculations by averaging over 60 states (i.e. $\text{SA-60-RASSCF}(4, 8|0, 0|4, 8)/\text{SS-RASPT2}$) to obtain the manifold of higher lying excited states accessible from the dark state and, thus, responsible for the visible ESA in the spectrum computed at longer waiting times. Within the RASPT2 calculations an imaginary level-shift correction of 0.2 au was used in order to avoid the presence of intruder states³⁷, the core orbitals were frozen. The CASPT2 standard zeroth-order Hamiltonian was used³⁴. For all computations the ANO-L basis set contracted to $\text{C}[3s, 2p, 1d]/\text{H}[2s1p]$ was used³⁸. The Cholesky decomposition was adopted to speed up the evaluation of two-electron integrals³⁹.

Minimal active space SA-2-CASSCF(2,2)/6-31G* mixed quantum-classical dynamics simulations were conducted in the L_a excited state for 250 fs with a time step of 0.5 fs, thereby employing zero initial starting velocity (i.e. a single $0K$ -trajectory). The small active space used in the dynamics simulations is necessary due to the inherent inability of CASSCF to describe the dark S_1 (L_b) and the bright S_2 (L_a) states at equal footing, which leads to the unphysical mixing of both states during the dynamics. Including solely the HOMO and the LUMO suppresses the description of the L_b state which additionally requires orbitals HOMO-1 and LUMO+1, while considering the L_a state which is characterized by a nearly pure $H \rightarrow L$ transition. Consequently, the minimal active space reveals solely the dynamics on the bright state and is blind for the state mixing in the L_b/L_a crossing region traversed during the simulation (see Results). Effectively, the single trajectory resembles more closely the diabatic picture, in which the nature of the ES is followed. We believe that for the particular study this quasi-diabatic description is suitable for two reasons: a) a crossing region between the bright and the dark states is encountered along the deformations dictated by the FC-active modes (see Results). As in the vicinity of a conical intersection the diabatic couplings are small, unlike the non-adiabatic couplings, the short-time dynamics are better described in the diabatic representation; b) the effective ES lifetime T_e , which we use, was obtained experimentally through fitting the decay of the transient ESA features at 550 nm^{40,41}, which are associated with the electronic configuration of the bright (i.e. the diabatic) state.

The ability of the CASSCF(2,2) dynamics to reproduce the main dynamical features of the L_a state of pyrene is discussed in detail in the Results section. Due to the overestimation of the energies at CASSCF(2,2) an ad-hoc scaling of the electronic gap was performed. A linear constant factor of 0.65 was extracted out of averaging over calculations at 50 auxiliary points along the L_a trajectory (i.e. structures at which the trend of the L_a energy changes) computed at SA-60-RAS(4, 8|0, 0|4, 8)/SS-RASPT2/ANO-L(321,21) level.

The electronic structure computations and geometry optimizations were performed with the Molcas 7.9 software⁴², while the quantum-classical dynamics was operated through the velocity Verlet algorithm implemented in the Cobramm software⁴³ and interfaced with Molcas 7.9.

Employing the computed SS-RASPT2 energies and the SA-RASSCF transition dipole moments (TDMs), absorptive 2D electronic spectra were computed by implementing eqs. 15-17 within the sum-over-state (SOS) framework⁴⁴ in a development version of Spectron 2.7²². In practice the $g - e$ coherence is modelled using eq. 12, where ω_k and D_k are extracted from the $0K$ -trajectory using a Fourier series to fit the temporal evolution of the electronic gap $E_e(t) - E_g(0)$, while the adiabatic transition ω_{eg} is set to the electronic gap between the GS equilibrium g and the lowest energy point passed during the first oscillation of the wavepacket propagating in the ES e . Regarding the evaluation of the $e - f$ coherence necessary to evaluate eq. 15 we assume that on an ultrashort time scale the wavepacket promoted with the probe pulse to a particular higher excited state will preserve its wavefunction character (diabatic representation). We selected at the FC point the states from the manifold of higher lying states f with significant oscillator strength out of the L_a state within the probed spectral window (i.e. the reference diabatic states) and tracked the temporal evolution of the wavefunction associated with each reference state along the 50 auxiliary points by searching for the adiabatic state with the greatest overlap with the reference, thereby considering only the CI-coefficients as the molecular orbitals change only slightly. The energy and TDM fluctuation profiles extracted in this way were subsequently fitted with Fourier series allowing to compute the required quantities for any temporal resolution. We stress here that tracking diabatic states in that way is only an approximate and not always unambiguous procedure. In the future we aim to interface a diabatization routine to the electronic structure computations, which will allow us to work directly in the diabatic representation, both for performing mixed quantum-classical dynamics simulations and for diabatic state tracking.

The effect of temporally finite pulses is not considered in this treatment, i.e. the spectra simulations are performed in the semi-impulsive limit. GSB and SE contributions appear as red peaks, while ESA appear as blue peaks in the 2D plots. A pure dephasing rate constant γ corresponding to 200 cm^{-1} was used.

4 Results

As outlined in the theoretical section, if the dephasing processes in the system occur on a time scale which is comparable to duration of the experiment, the spectra reveal an averaged picture of the dynamics during the measurement. Therefore, the main photoinduced phenomena caused by the irradiation with the pump and probe laser pulses must be known in order to simulate linear and nonlinear spectroscopy. In the following, we characterize the photophysics and photochemistry of

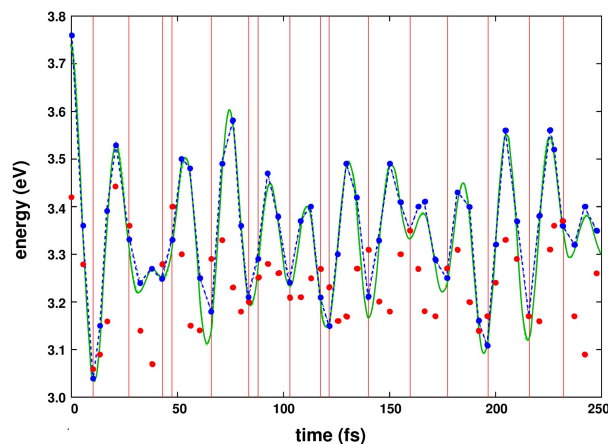


Fig. 3 Fluctuation of the L_a -GS vertical gap along the scaled CAS(2,2)/6-31G* dynamics of pyrene on the bright L_a state (green line). A constant scaling factor of 0.65 was derived by performing high level RAS(4, 8|0, 0|4, 8)/SS-CASPT2 computations at 50 geometries along the trajectory (8-10 fs, 26-28 fs, 44-46 fs, etc.). The energies of the L_a and the L_b states (obtained from the high level calculation) at these geometries are marked with red and blue dots, respectively. At several occasions along the trajectory (marked by red lines) a near-degeneracy and even inversion of the energies of the L_a and L_b states is observed indicating the vicinity of the crossing region.

pyrene.

The GS minimum, hereafter denoted as $^1(\text{gs})_{\text{min}}$, belongs to the D_{2h} point group. The FC point is characterized by two low-lying singlet excited states. Following Platt's nomenclature³⁶, S_1 is the so-called L_b state, whose wave function is described by the negative linear combination of the $H \rightarrow L+1$ and $H-1 \rightarrow L$ configurations, while S_2 is referred to as the L_a state, having a wave function dominated by the $H \rightarrow L$ configuration. The L_b and L_a vertical excitation energies at the FC point are equal to 3.42 and 3.77 eV, respectively (see †, Table S1). The electronic transition from the ground state to the L_b state is dark within D_{2h} symmetry, while the L_a absorption is characterized with a high oscillator strength of 0.17. This implies that the interaction of the system with near-UV radiation causes the population of solely the L_a state, from which consequently the main photoinduced events of the system take place.

In order to study the L_a photophysics, a SA-CASSCF(2,2)/6-31G* mixed quantum-classical dynamics simulation with zero starting velocity was conducted starting at the FC point (Figure 3, green line). A legitimate question is whether such a limited computational level could describe the essential dynamics on the L_a state with a sufficient accuracy. From experimental observations, it is known that after excitation into the L_a state an ultrafast population transfer toward the L_b state takes place with a time constant of 85 fs¹⁹. As the time is too short to allow for vibrational energy redistribution, a conical intersection (CI) between the L_a and L_b state must be encountered along the deformations dictated by the FC active modes. Therefore, the quality of the dynamics can be assessed by analyzing if pyrene explores regions of near degeneracy between the L_a and the L_b states. Full RASSCF(4, 8|0, 0|4, 8)/RASPT2 computations at 50 auxiliary points along the trajectory, which provide the energies of both L_b and L_a demonstrate that both states swap order multiple times (marked in Figure 3 with red vertical lines), with the state crossing being reached for the first time

after less than ~ 10 fs. In fact, the region of inverted state order is visited by the molecule ca. every 20 fs (8-10 fs, 26-28 fs, 44-46 fs, etc.).

The minimum on the L_a surface in D_{2h} symmetry is found about 0.5 eV beneath the FC point and is characterized by the equilibration of the conjugated bonds in the periphery of pyrene (Figure 4, ${}^1(L_a)_{\min}$, see also †, Table S1). The most pronounced bond variations are around 0.04-0.05 Å. The analysis of several geometries in the region of inverted state order (see †, Figures S2 and S3) demonstrates that the crossings appear within 0.2-0.4 eV above ${}^1(L_a)_{\min}$, thus being below the FC limit of 3.77 eV. The crossings are characterized by a more pronounced displacement along the very same coordinate that connects the FC point to ${}^1(L_a)_{\min}$, with bond variations up to 0.05-0.07 Å. Accordingly, the CIs lie closer to the outer turning point along this coordinate.

Based on the above findings we postulate a simple one-dimensional model that comprises the ultra fast photophysics of pyrene (Figure 4). After irradiation the populated bright L_a state undergoes a sub-10 fs bond length relaxation. The momentum accumulated in the FC active modes drives the system beyond the L_a minimum to a turning point, which lies in the vicinity of the L_a/L_b crossing region. The wavepacket bifurcates and a part continues its dynamics on the L_b surface, while the wavepacket that remains on the L_a surface makes one turn in order to return to the crossing region ca. every 20 fs. The efficiency of the transfer could be roughly estimated to 15% (assuming that within 85 fs the wavepacket reaches the CI region five times, a constant $L_a \rightarrow L_b$ population transfer rate and neglecting population transfer back to L_a). It is well known from earlier transient spectroscopy studies with picosecond resolution that the pyrene is trapped in the L_b minimum (Figure 4, ${}^1(L_b)_{\min}$, see also †, Table S1) before it eventually decays to the ground state through fluorescence^{40,45} (L_b lifetime 339 ns⁴¹). To summarize, the obtained results clearly demonstrate that the CASSCF(2,2) dynamics grasps the essential dynamics along the L_a state responsible for reaching the CI region.

We now turn to the electronic spectroscopy of pyrene. First we present the linear absorption (LA)

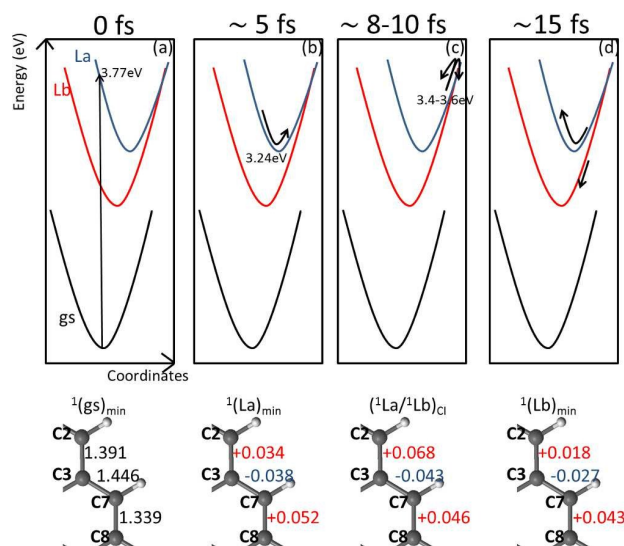


Fig. 4 Schematic representation of the photophysics of pyrene based on the $0K$ -trajectory dynamics augmented by high level electronic structure computations at relevant points. The dominant bond deformations are given, with the GS equilibrium geometry used as a reference.

spectrum, which is obtained by a Fourier transformation of the first order response function given by

$$R^{(1)}(t) = i|\mu_{eg}|^2 e^{-i\omega_{eg}t + g(t) - \Gamma t} \quad (18)$$

The electronic energy gap fluctuations due to the lineshape function $g(t)$ are obtained through fitting the dynamics with a Fourier series as outlined in the Computational Methods. The homogeneous broadening $\Gamma = \gamma + 1/T_e$ is affected by two contributions, a lifetime broadening with a relaxation rate constant $1/T_e = 1/85$ fs (corresponds to a 125 cm^{-1} Lorentzian bandwidth), which accounts for the decay from the bright L_a state to the dark L_b state^{19,46}, and a pure dephasing rate constant γ which accounts for signal decay due to solute-solvent interactions.

The fit reveals that the initial relaxation dynamics of pyrene can be described through a few dom-

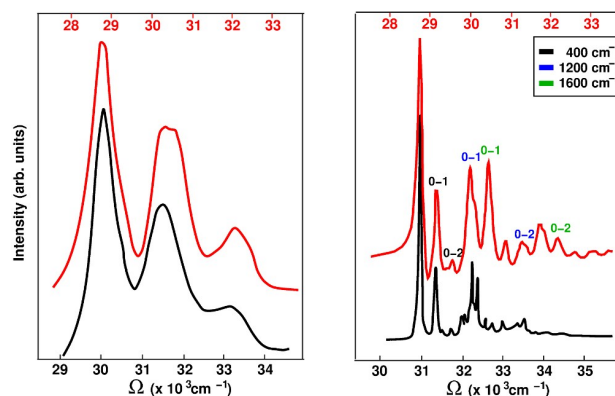


Fig. 5 Comparison of the experimental (black line) and theoretical (red line) linear absorption spectrum of pyrene recorded in aqueous solution at room temperature (left) and in a Ne-matrix at 6K (right). The theoretical and experimental spectra are normalized with respect to the fundamental (0-0) transition. The spectral bandwidth was modeled through a lifetime broadening parameter of 125 cm^{-1} (corresponds to the 85 fs lifetime of the L_a state). Additionally, a dephasing rate constant of 200 cm^{-1} was used for the aqueous spectrum to model fluctuations due to solute-solvent interactions. The overtones of the three dominant modes which contribute to the vibrational progression are labeled.

inant vibrational modes, a 400 cm^{-1} , a 1200 cm^{-1} and 1600 cm^{-1} mode with Huang-Rhys factors 0.46, 0.44 and 0.41, superimposed with several less intense modes. These modes match well the ones reported by Freidzon et. al to have the highest L_a Huang-Rhys factors in gas-phase (412 cm^{-1} (0.26), 1277 cm^{-1} (0.214), 1456 cm^{-1} (0.219), 1700 cm^{-1} (0.279), Huang-Rhys factors in parenthesis)⁴⁷ out of ab initio LA spectra generated within the Franck-Condon and Herzberg-Teller approximations. Freidzon et. al also report that similar modes are responsible for the vibronic profile of pyrene in water, based on computations of pyrene clustered by 44 waters, which represent its first solvation shell.

The vibrational modes with the highest Huang-Rhys factors contribute to the vibrational progression, which gives the spectral lineshape of the absorption spectrum. Figure 5, left panel, compares the theoretical spectrum (red), based on the dynamics simulation in vacuo, and the experimental spectrum (black), obtained in aqueous solution⁴⁸. The rate constant γ was set to 200 cm^{-1} to fit the bandwidth of the solvated spectrum. Both spectra show a vibrational progression with three absorption peaks with origin around 30000 (29000) cm^{-1} (i.e. the adiabatic transition energy ω_{eg}). The

vibrational bands are separated by $\sim 1400 \text{ cm}^{-1}$, with the 0-0 transition accumulating the highest oscillator strength. Figure 5, right panel, compares the theoretical spectrum (red) and the experimental spectrum (black) recorded in a Ne-matrix at 6K⁴⁹. Thereby, the pure dephasing rate constant γ was set to zero. Both spectra exhibit a finer vibronic structure, which reveals the progression due to the 400 cm^{-1} mode, not visible in the LA spectrum in solution. Notably, the theoretical spectrum characterizes with larger weights for the 0-2 overtones and a red-shift of the 0-0 transition of $\sim 2200 \text{ cm}^{-1}$, which is within the accuracy limits of the RASSCF/RASPT2 protocol and is probably due to the low level dynamics and the use of a uniform scaling factor. It should be noted as well that the pyrene absorption bands exhibit a red-shift of 1000 cm^{-1} in water⁴⁸.

The LA spectrum of pyrene reveals the FC-active modes that govern the immediate excited state dynamics. However, changes of the electronic structure due to population transfer among excited states remain hidden. Ultrafast transient electronic spectroscopy provides the missing information. Each electronic state possesses characteristic bright transitions which give rise to ESA peaks in the transient spectra and can be used for state recognition. Pyrene is no exception to this rule, the bright L_a and the dark L_b states have essentially different electronic structure, therefore probing the initial ultrafast dynamics on the L_a state has different signatures than the subsequent dynamics in the L_b state^{41,46}. To demonstrate this we generate the 2DUV spectra of pyrene and their marginals (i.e. the pump-probe spectra), for two different waiting time t_2 . For simulating the so called FC spectrum we assume that pump (second pump pulse in the case of 2D spectroscopy) and probe pulse arrive simultaneously at the sample, i.e. $t_2 = 0$. This spectrum should reveal the ESA transitions associated with the dynamics of the wavepacket on the L_a surface. Another set of spectra is generated for a waiting time t_2 on the picosecond time scale and resolves the ESAs of the L_b state.

The vertical SA-60-RASSCF(4, 8|0, 0|4, 8)/SS-RASPT2 transitions at 50 auxiliary points along the

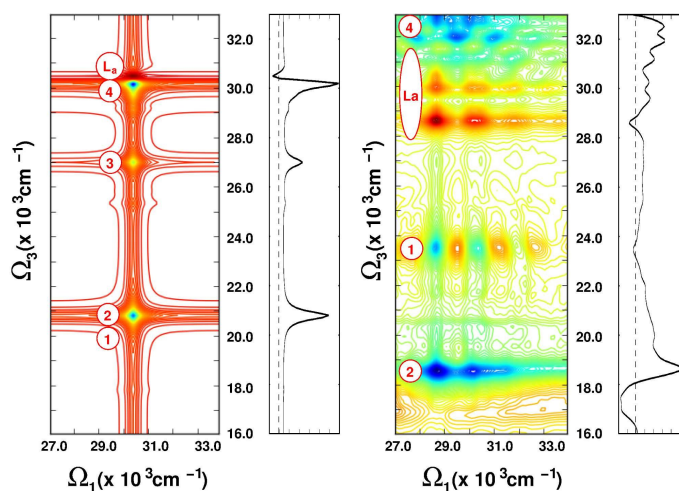


Fig. 6 Theoretical quasi-absorptive 2D electronic spectrum of pyrene for a delay time $t_2 = 0$: left) applying the snapshot approximation for the coherence evolution during t_1 and t_3 ; right) applying eq. 15, thus explicitly including spectral diffusion during the coherence times t_1 and t_3 . The marginals of the 2D electronic spectra (i.e. the pump-probe spectra), obtained through integration over Ω_1 , are depicted on the side. Peaks assignment is performed for the most characteristic transitions. The excited states associated with these transitions are given in Table 1

scaled CAS(2,2) $0K$ -trajectory, together with the associated TDMs, provide the required quantities for constructing the FC 2D spectrum of pyrene. We compare two different computational strategies. Assuming (unrealistically) that the time-scale for ES relaxation is much longer compared to the duration of the experiment we apply the snapshot approximation for simulating the coherence evolution during the delay times t_1 and t_3 and model the broadening of all optical transitions with a constant uniform Lorentzian linewidth (Figure 6, left). On the other hand, the spectral lineshape in Figure 6, right, incorporates the fluctuations of the electronic gap during the delay times t_1 and t_3 through the use of eq. 15. Prominent transitions are labeled (L_a GSB/SE, peaks 1-4). Apart from the obvious inability of the static approach to reproduce the vibronic structure of the GSB, the comparison between both levels of theory clearly demonstrates that the static approximation reproduces the positions of the ESA only qualitatively, thereby neglecting the dynamically induced blue/red-shift and the peak broadening. We draw the reader's attention to two observations: first, while peaks 1,3 and 4 blue-shift (by up to 4000 cm^{-1}) when the fluctuation of the electronic gap is considered, peak 2 exhibits a pronounced red-shift of $\sim 2000\text{ cm}^{-1}$; second, peaks 1 and 4 whose wavefunctions are dominated by the negative (respectively positive) linear combination of the $H-4 \rightarrow L+1$ and $H-1 \rightarrow L+4$ configurations, both blue-shift, with the negative linear combination, which is dark in the FC region, gaining oscillator strength on the expense of the positive linear combination, which is covered by the GSB/SE.

The 2D spectrum in Figure 6 recovers the vibrational structure of the GSB along ω_1 and ω_3 , with

Table 1 Vertical excitation energies ΔE (in eV and cm^{-1}), transition dipole moments (in a.u.) out of the L_a and wavefunctions for excited states responsible for the computed ESA peaks appearing in the spectra in Fig. 6.

label	ΔE (from L_a)		TDM	conf.	coeff.
	eV	cm^{-1}			
1	2.36	19034	0.00	$H-4 \rightarrow L+1$	0.48
				$H-1 \rightarrow L+4$	-0.33
				$H-1 \Rightarrow L+1$	0.31
				$H-1, H \Rightarrow L, L+1$	-0.28
2	2.58	20809	1.97	$H \Rightarrow L$	0.33
				$H-1, H \Rightarrow L, L+1$	0.29
				$H \rightarrow L+3$	0.29
				$H-1 \Rightarrow L+1$	0.26
				$H-2, H \Rightarrow L, L+2$	0.26
3	3.35	27029	1.28	$H-4 \rightarrow L+1$	0.44
				$H-1 \rightarrow L+4$	0.40
				$H \Rightarrow L+1$	0.27
4	3.75	30246	2.54	$H-1 \rightarrow L+4$	0.32
				$H-3 \rightarrow L$	-0.31
				$H-1 \Rightarrow L$	0.29
				$H \Rightarrow L$	-0.26

the third vibronic band (i.e. the 0-2 overtone) along ω_3 being covered by a close lying intense ESA. Three characteristic ESAs appear in the spectrum at 18500 cm^{-1} (peak 2), 23500 cm^{-1} (peak 1) and

33000 cm^{-1} (peak 4). ESA peak 2 is responsible for the intense absorption, observed in transient pump-probe spectra with high temporal resolution (30-60 fs)^{19,46} around 17000-18000 cm^{-1} , and constitutes the most characteristic signature of the S_1 state in the Vis. A weak absorption band around 25000 cm^{-1} , reported by Krebs *et al.*⁴¹, matches the position of peak 1. To the best of our knowledge no transient data with sufficient temporal resolution that probes beyond 32000 cm^{-1} has been reported in the literature, therefore it appears that intense absorption associated with peak 4 has not been detected yet.

The performed ab initio quantum-chemical calculations allow us to characterize the nature of the

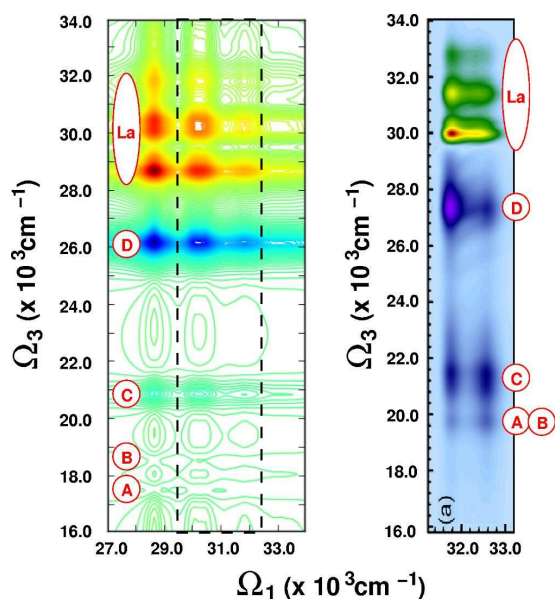


Fig. 7 Theoretical (left) and experimental (right) quasi-absorptive 2D electronic spectrum of pyrene for a delay time t_2 in the picosecond range ($t_2 = 1$ ps in the experiment) obtained through pumping at the frequency of the S_2 transition and supercontinuum probing in the Vis-to-UV. In the simulation all vibrational bands of the $GS \rightarrow S_2$ transitions are excited, while in the experiment the fundamental is suppressed. In the simulation it is assumed that probing occurs from the minimum on the dark S_1 $^1(L_b)_{\min}$, which is populated with a time constant of 85 fs and where the system is trapped on a time scale much longer than the experiment. The vertical transitions along ω_3 are obtained from a single point SA-60-RASSCF(4, 8|0, 0|4, 8)/SS-RASPT2 calculation at $^1(L_b)_{\min}$. Peaks assignment is performed for the most characteristic transitions. The excited states associated with these transitions are given in Table 2. The experimental spectrum is taken from¹⁹.

electronic excited state giving rise to the fingerprint ESA at 18000 cm^{-1} (peak 2, see also Table 1). The dominant configurations can be described in the language of vibrational spectroscopy as the overtone of the $GS \rightarrow L_a$ transition, i.e. $H \Rightarrow L \equiv H \rightarrow L + H \rightarrow L$. The doubly excited state appears red-shifted with respect to the sum of the single electron transitions out of the GS, a large anharmonicity of 1 eV is observed. Our computations reveal that the energy of the overtone transition decreases from the FC towards the $^1(L_a)_{\min}$ due to the larger stabilization of the doubly excited state in comparison to the L_a state. This unique feature of overtones, documented by us for other systems as well⁸, causes peak 2 to red-shift by nearly 2000 cm^{-1} when dynamic fluctuation are considered in

the simulation of the spectrum and explains the overestimation of the ESA transition in the static spectrum (21000 cm^{-1} in Figure 6, left) compared to the experimental findings (17000 cm^{-1} ^{41,46}).

We now turn our attention to the spectrum at waiting time t_2 in the picosecond range. On the basis

Table 2 Vertical excitation energies ΔE (in eV and cm^{-1}), transition dipole moments (in a.u.) out of the L_b and wavefunctions for excited states responsible for the computed ESA peaks appearing in the spectrum in Fig. 7.

label	ΔE (from L_b)		TDM	conf.	coeff.
	eV	cm^{-1}			
A	2.16	17442	0.66	H-3 \rightarrow L	0.50
				H \rightarrow L+3	0.48
B	2.29	18452	0.56	$\bar{H}-1 \rightarrow \bar{L}+2$	0.53
				H-2 \rightarrow L+1	-0.48
C	2.58	20787	0.65	$\bar{H} \Rightarrow \bar{L}, \bar{L}+1$	0.51
				H-1, H \Rightarrow L	0.28
D	3.24	26132	1.55	$\bar{H}-1, \bar{H} \Rightarrow \bar{L}+1$	0.36
				H-1, H \Rightarrow L	-0.32
				H \Rightarrow L, L+1	-0.32
				H-1 \Rightarrow L, L+1	0.31
				H-1 \rightarrow L+3	0.30
				H-3 \rightarrow L+1	-0.30

of the available literature on pyrene, it is evident that after 1 ps the excited state population has decayed to the dark L_b state minimum $^1(L_b)_{\text{min}}$ where it remains trapped on a time scale much longer than the duration of the experiment^{40,41,45}. Consequently, the appearing ESA signals are caused by electronic promotion out of the $^1(L_b)_{\text{min}}$. Employing SS-RASPT2 energies and the SA-RASSCF TDMs at the $^1(L_b)_{\text{min}}$ we constructed the 2D spectrum for these conditions by coupling the short-time dynamics to the static description of the dark state intermediate (Figure 7, left panel). We remind that this approach does not require information about the coherent dynamics during t_2 and should be applied only for generating the spectra of excited state intermediates, which are expected to trap the population for a sufficiently long time.

The simulated spectrum recovers the vibrational structure of the GSB, as well as two distinct ESA peaks at $\sim 21000\text{ cm}^{-1}$ and $\sim 26000\text{ cm}^{-1}$ (C, D in Figure 7). Two less intensive peaks (A, B in Figure 7) appear around 18000 cm^{-1} . Next, we elucidate the nature of excited states responsible for these ESA signals through analysis of the corresponding RASSCF wave functions. The latter are reported in Table 2. To underline that different states are revealed with respect to the FC spectrum (Figure 6) we use letter-code to label the ESA peaks in Figure 7. The excited states associated with both most intense ESA peaks C and D can be regarded as combination bands of the lowest singly excited states of pyrene (L_a , L_b , B_a , B_b in Platt's notation³⁶). The excited state giving rise to peak C can be seen as L_b+L_a transition, while the state associated with peak D as L_b+B_a transition. As in the FC spectrum, the transitions exhibit pronounced anharmonicities and appear strongly red-shifted with respect to the sum of the single electron transitions which assemble them. The states associated with two less intense ESA peaks A and B are described by singly excited configuration

state functions involving H-3/L+3 (peak A) as well as H-2/L+2 (peak B).

Riedle and co-workers reported recently an experimental 2D electronic spectrum of pyrene in methanol, recorded in a collinear pump-probe set-up utilizing a narrowband pump-pulse pair, centered around 32000 cm^{-1} , i.e. at the second and third vibrational bands of the L_a absorption and a supercontinuum probe pulse covering the Vis-to-UV spectral window ($16000\text{-}38000\text{ cm}^{-1}$ ¹⁹). A time delay t_2 equal to 1 ps was used. Such a result represents one of the few experimental examples employing Vis-UV broad pulses for 2D spectroscopy. The spectrum is shown in Figure 7, right panel. Through the use of a narrowband pump-pulse pair the fundamental (0-0) was suppressed along ω_1 , whereas it was recovered along ω_3 thanks to the supercontinuum probing. The ESA peaks do not exhibit a vibrational structure along ω_3 , but are noticeably elongated. The short lifetimes of the higher excited states or/and the large FC factors for the fundamental (0-0) transition could rationalize the broad and unstructured lineshapes. Knowledge of the energetic profiles of the higher excited states is necessary to shed more light on the matter. The comparison between theory and experiment shows an overall good agreement, which supports the validity of the applied approximations. On the basis of the ab initio quantum-chemical calculations it is now possible to unambiguously assign the bright ESA transitions C and D, while it can be speculated that peaks A and B characterize the weak ESA at 20000 cm^{-1} .

5 Conclusion

Bond length relaxations, the initial relaxation process in electronically excited molecular systems, are an immediate consequence of the altered electronic structure upon excitation and almost always occur on an ultrafast time scale. With the emerging laser technologies, approaching sub-fs pulse duration⁵⁰⁻⁵⁴, the signatures of the relaxation dynamics, governed by the FC-active modes, become visible. While these modes could be evaluated directly from ab initio computations using the time-(in)dependent Franck-Condon and Herzberg-Teller approximations or by fitting experimentally available high resolution LA spectra, the present approach, based on a mixed quantum-classical dynamics simulations, allows to simultaneously record the fluctuations of the higher excited states as a function of the dynamics in the photoactive state(s). In that sense the present contribution is an improvement of our previously presented strategy⁹ for incorporating higher excited states and is a further step towards the formulation of a computational protocol for the accurate computation of two-dimensional electronic spectra.

The present example of the ultrafast decay of pyrene from the bright L_a state to the dark L_b state probed for waiting times $t_2 = 0$ and $t_2 = 1$ ps demonstrates the shortcomings of the static description and the ability of the proposed approach to model ESA fluctuations and realistic lineshapes. Without the explicit consideration of electronic fluctuations due to the nuclear degrees of freedom the vibronic structure and spectral shifts of the peaks are neglected. The presented strategy couples accurate computations of the high-lying excited state manifold to dynamics simulations in molecular systems. The good agreement with the experimental results validates the formulated theoretical model.

Beyond the presented example the single trajectory approximation (eq. 15), in cooperation with multi-dimensional spectroscopy, can find application in resolving the spectral signatures of different

ground state conformers^{55,56}, as well as in tracking the photochemistry/photophysics on multiple bright states which are simultaneously excited in the FC region (e.g. the L_b , L_a , $n\pi^*$ states in native DNA and its building blocks^{8,57,58}). In the case of slow ES dynamics that are beyond the reach of mixed quantum-classical dynamics (i.e. longer than 1 ps) we demonstrated that short-time dynamics can be coupled to a static description of ES intermediates, which benefits from the computation of solely the excited state manifold at given representative geometries.

The single trajectory approach has its limitations. While reproducing spectral fluctuations of signals associated with the photoactive state it does not account for the emerging of transient signals due to non-adiabatic coupling to other states when the waiting time t_2 is comparable to the lifetime of the initially excited state. This shortcoming could be overcome by extending the current approach to a swarm of trajectories and propagating the complex amplitudes $c_i(t)$ according to the equations of motion 7 (instead of the simplified eqs. 9), thus, allowing to additionally incorporate non-adiabatic transitions among electronic states using Tully's fewest switches surface hopping^{2,3} as recently demonstrated by Jansen and coworkers². Dephasing rates and lifetimes will then naturally arise from the trajectory averaging at the expense of a substantially increased computational cost due to the calculation of a) multiple independent trajectories; b) the energy profiles of the higher excited states along each trajectory.

6 Acknowledgement

M.G. acknowledges support by the European Research Council Advanced Grant STRATUS (ERC-2011-AdG No. 291198). S.M. gratefully acknowledges the support of the National Science Foundation through Grant No. CHE-1361516 and the Chemical Sciences, Geosciences, and Biosciences division, Office of Basic Energy Sciences, Office of Science, U.S. Department of Energy. A.G. acknowledges financial support from Italian Ministry of Education and Research (MIUR)-Grant No. RBFR1248UI. B.P.F. gratefully acknowledges support through the German Research Foundation (DFG) within the Emmy Noether Programme (FI 2034/1-1). A.N. wishes to acknowledge the help of the Hamiltonian of Design studio (<http://hamiltonianofdesign.worldpress.com>) for creating the graphical abstract.

References

- 1 M. Sulc, H. Hernandez, T. J. Martinez and J. Vanicek, *J. Chem. Phys.*, 2013, **139**, 034112.
- 2 R. Tempelaar, C. P. van der Vegte, J. Knoester and T. L. C. Jansen, *J. Chem. Phys.*, 2013, **138**, 164106.
- 3 A. S. Petit and J. E. Subotnik, *J. Chem. Phys.*, 2014, **141**, 014107.
- 4 T. Zimmermann and J. Vanicek, *J. Chem. Phys.*, 2014, **141**, 134102.
- 5 A. Nenov, I. Rivalta, G., S. Mukamel and M. Garavelli, *Comput. Theor. Chem.*, 2014, **1040**, 295.
- 6 Z. Li, D. Abramavicius and S. Mukamel, *J. Am. Chem. Soc.*, 2008, **130**, 3509–3515.
- 7 I. Rivalta, A. Nenov, O. Weingart, G. Cerullo, G., S. Mukamel and M. Garavelli, *J. Phys. Chem. B*, 2014, **118**, 8396.
- 8 A. Nenov, J. Segarra-Martí, A. Giussani, I. Conti, I. Rivalta, E. Dumont, V. K. Jaiswal, S. F. Altavilla, S. Mukamel and M. Garavelli, *Faraday discussions*, 2015.
- 9 I. Rivalta, A. Nenov, G. Cerullo, S. Mukamel and M. Garavelli, *Int. J. Quantum Chem.*, 2014, **114**, 85–93.
- 10 A. N. A. Giussani, J. Segarra-Martí, V. K. Jaiswal, I. Rivalta, G. Cerullo, S. Mukamel and M. Garavelli, *J. Chem. Phys.*, 2015, accepted.

- 11 C. H. Tseng, S. Matsika and T. C. Weinacht, *Opt. Express*, 2009, **17**, 18788–18793.
- 12 A. H. V. I. Prokhorenko and R. J. D. Miller, *Opt. Express*, 2009, **17**, 9764.
- 13 B. A. West and A. M. Moran, *J. Phys. Chem. Lett.*, 2012, **3**, 2575–2581.
- 14 S. Ruetzel, M. Kullmann, J. Buback, P. Nuernberger and T. Brixner, *Phys. Rev. Lett.*, 2013, **110**, 148305.
- 15 F. Koch, M. Kullmann, U. Selig, P. Nuernberger, D. C. G. Gotz, G. Bringmann and T. Brixner, *New J. Phys.*, 2013, **15**, 025006.
- 16 A. F. Fidler, V. P. Singh, P. D. Long, P. D. Dahlberg and G. S. Engel, *Nature Commun.*, 2014, **5**, 3286.
- 17 J. R. Widom, N. P. Johnson, P. H. von Hippel and A. H. Marcus, *New J. Phys.*, 2013, **15**, 025028.
- 18 A. Halpin, P. J. M. Johnson, R. Tempelaar, R. S. Murphy, J. Knoester, T. L. C. Jansen and R. J. D. Miller, *Nature Chem.*, 2014, **6**, 196–201.
- 19 N. Krebs, I. Pugliesi, J. Hauer and E. Riedle, *New J. Phys.*, 2013, **15**, 085016.
- 20 S. Mukamel, *Principles of Nonlinear Optics and Spectroscopy*, Oxford University Press, Oxford, UK, 1995.
- 21 P. Hamm and M. Zanni, *Concepts and Methods of 2D Infrared Spectroscopy*, Cambridge University Press, Cambridge, UK, 2011.
- 22 D. Abramavicius, B. Palmieri, D. V. Voronine, F. Sanda and S. Mukamel, *Chem. Rev.*, 2009, **109**, 2350–2408.
- 23 A. W. Jasper, C. Zhu, S. Nangia and D. G. Truhlar, *Faraday Discuss.*, 2004, **127**, 1.
- 24 M. T. U. Muller, *J. Chem. Phys.*, 1997, **107**, 6230.
- 25 B. R. Landry and J. E. Subotnik, *J. Chem. Phys.*, 2013, **137**, 22A513.
- 26 A. Kelly and T. E. Markland, *J. Chem. Phys.*, 2013, **139**, 064316.
- 27 F. F. de Carvalho, M. E. F. Bouduban, B. F. E. Curchod and I. Tavernelli, *Entropy*, 2014, **16**, 62.
- 28 M. Barabatti, R. Shepard and H. Lischka, *Conical Intersections: Theory, Computation and Experiment*, World Scientific, Singapore, 2011, vol. 17.
- 29 J. C. Tully, *J. Chem. Phys.*, 1990, **93**, 1061.
- 30 K. E. Dorfman, B. P. Fingerhut and S. Mukamel, *Phys. Chem. Chem. Phys.*, 2013, **15**, 12348.
- 31 B. O. Roos, P. R. Taylor and P. E. M. Siegbahn, *Chem. Phys.*, 1980, **48**, 157.
- 32 B. O. Roos, *Ab Initio Methods in Quantum Chemistry: part II*, Wiley, Chichester, UK, 1987.
- 33 K. Andersson, P. A. Malmqvist, B. O. Roos, A. J. Sadlej and K. Wolinski, *J. Phys. Chem.*, 1990, **94**, 5483–5488.
- 34 G. Ghigo, B. O. Roos and P. A. Malmqvist, *Chem. Phys. Lett.*, 2004, **396**, 142–149.
- 35 P. A. Malmqvist, A. Rendell and B. O. Roos, *J. Phys. Chem.*, 1990, **94**, 5477.
- 36 J. R. Platt, *J. Chem. Phys.*, 1949, **17**, 484.
- 37 N. Forsberg and P. A. Malmqvist, *Chem. Phys. Lett.*, 1997, **274**, 196–204.
- 38 P. O. Widmark, P. A. Malmqvist and B. O. Roos, *Theor. Chim. Acta*, 1990, **77**, 291–306.
- 39 F. Aquilante, T. B. Pedersen and R. Lindh, *Theor. Chem. Acc.*, 2009, **124**, 1.
- 40 F. V. R. Neuwahl and P. Foggi, *Laser Chem.*, 1999, **19**, 375.
- 41 N. Krebs, *PhD Thesis*, 2013, Ludwig–Maximilians–Universität München.
- 42 F. Aquilante, L. De Vico, N. Ferre, G. Ghigo, P. A. Malmqvist, P. Neogrady, T. B. Pedersen, M. Pitonak, M. Reiher, B. O. Roos, L. Serrano-Andrés, M. Urban, V. Veryazov and R. Lindh, *J. Comput. Chem.*, 2010, **31**, 224.
- 43 P. Altoè, M. Stenta, A. Bottoni and M. Garavelli, *Theor. Chem. Acc.*, 2007, **118**, 219.
- 44 G. H. Chen, S. Mukamel, D. Beljonne and J. L. Bredas, *J. Chem. Phys.*, 1996, **104**, 5406–5414.
- 45 P. Foggi, L. Pettini, I. Santa, R. Righini and S. Califano, *J. Phys. Chem.*, 1995, **99**, 7439.
- 46 M. Raytchev, E. Pandurski, I. Buchvarov, C. Modrakowski and T. Fiebig, *J. Phys. Chem. A*, 2003, **107**, 4592.
- 47 A. Y. Freidzon, R. R. Valiev and A. A. Berezhnuy, *RSC Adv.*, 2014, **4**, 42054.
- 48 F. P. Schwartz and S. P. Wasik, *Anal. Chem.*, 1976, **48**, 524.
- 49 T. M. Halasinski, F. Salama and L. J. Allamandola, *Astrophys. J.*, 2009, 56.
- 50 P. Baum, S. Lochbrunner and E. Riedle, *Opt. Lett.*, 2004, **29**, 1686.
- 51 K. Kosma, S. A. Trushin, W. E. Schmid and W. Fuss, *Opt. Lett.*, 2008, **33**, 723.
- 52 U. Graf, M. Fiess, M. Schultze, R. Kienberger, F. Krausz and E. Goulielmakis, *Opt. Express*, 2008, **16**, 18956.
- 53 Y. Kida, J. Liu, T. Teramoto and T. Kobayashi, *Opt. Lett.*, 2010, **35**, 1807.

-
- 54 R. B. Varillas, A. Candeo, D. Viola, M. Garavelli, S. D. Silvestri, G. Cerullo and C. Manzoni, *Opt. Lett.*, 2014, **39**, 3849.
- 55 A. Nenov, I. Rivalta, G. Cerullo, S. Mukamel and M. Garavelli, *J. Phys. Chem. Lett.*, 2014, **5**, 767.
- 56 A. Nenov, S. a Beccara, I. Rivalta, G. Cerullo, S. Mukamel and M. Garavelli, *ChemPhysChem*, 2015, **15**, 3282.
- 57 B. P. Fingerhut, K. E. Dorfman and S. Mukamel, *J. Phys. Chem. Lett.*, 2013, **4**, 1933.
- 58 B. P. Fingerhut, K. E. Dorfman and S. Mukamel, *J. Chem. Theor. Comput.*, 2014, **10**, 1172.